Research Article | Vol. 33, No. 13 / 30 Jun 2025 / Optics Express 27043
Optics EXPRESS

Probing linewidth dynamics with short-time delayed linear interferometer in integrated frequency microcombs

WENTING WANG,[1,2,6,†] DONG IL LEE,[1,†] WENZHENG LIU,[1,†] MINGBIN YU,[3,4] DIM-LEE KWONG,[4] NINGHUA ZHU,[5] AND CHEEWEI WONG[1,7]

[1]*Fang Lu Mesoscopic Optics and Quantum Electronics Laboratory, University of California, Los Angeles, California 90095, USA*
[2]*Mesoscopic Optics and Advanced Instruments Laboratory, School of Optics and Photonics, Beijing Institute of Technology, Beijing 100081, China*
[3]*State Key Laboratory of Functional Materials for Informatics, Shanghai Institute of Microsystem and Information Technology, Shanghai 200050, China*
[4]*Advanced Micro Foundry, Singapore 117685, Singapore*
[5]*Institute of Intelligent Photonics, NanKai University, Tianjin 300457, China*
[6]*wentingwang@ucla.edu*
[7]*cheewei.wong@ucla.edu*
[†]These authors contributed equally to this work.

Abstract: Optical frequency microcombs generate a series of equidistant, coherent frequency references over a broad spectrum, advancing spectroscopy, communications, metrology, and astronomy. Here, we design and fabricate a silicon nitride adiabatic ring microresonator that achieves low average dispersion with negligible avoided mode crossings. We explore the soliton microcomb bifurcation diagram for various mode-locking states in the microresonator, and investigate the stochastic linewidth through both numerical simulations and experimental measurements. The fabricated microresonator exhibits a loaded quality factor of 1.8 million, a measured group velocity dispersion of -3 ± 1.1 fs^2/mm, and a free spectral range of 88 GHz, characterized using swept-wavelength interferometry. We experimentally demonstrate thermally stabilized microcomb formation in the device using a dual-polarization-driven method, enabling access to single soliton, double soliton, and soliton crystal microcombs with forward and backward pump wavelength tuning. A short-time delayed linear interferometer is developed to examine the linewidths of individual comb teeth and the soliton microcomb linewidth distributions. The measured interferometric envelopes for the single-soliton, double-soliton, and soliton crystal microcombs show linewidths of 2.3 kHz, 3.0 kHz, and 2.4 kHz, respectively. The linewidth distribution broadens slightly away from the pump towards shorter wavelengths, exhibiting increased fluctuations due to the structured optical spectrum. Understanding the fundamental linewidths in high-clock-rate frequency microcombs is essential for unlocking new applications.

1. Introduction

The optical frequency comb has revolutionized ultrafast optics over the past two decades, thanks to its equidistant spectral lines, which serve as highly accurate frequency Refs. [1]. Among various implementations, frequency microcombs have garnered significant attention due to their compact size, low power consumption, and potential for scalable photonic integration [2]. Driven by light confined in ultrahigh-quality-factor (Q) microresonators [3], soliton microcombs offer broad spectral bandwidth and high individual comb line power by balancing Kerr nonlinearity and dispersion across various platforms [4–7]. Recently, microcombs have demonstrated remarkable versatility, finding applications in dual-comb precision spectroscopy [8], high-capacity optical

#558703 https://doi.org/10.1364/OE.558703
Journal © 2025 Received 3 Feb 2025; revised 14 May 2025; accepted 14 May 2025; published 17 Jun 2025

Optics EXPRESS

communications [9], precision metrology [10], as well as ultra-stable microwave [11–13] and THz generation [14,15]. Moreover, integrating microcombs into silicon photonics platforms holds the promise of developing multifunctional photonic circuits that combine high spectral purity with unprecedented miniaturization [16–18], paving the way for next-generation integrated photonic devices to meet the demands of technological frontiers.

Parallel to these advancements, the linewidth and phase noise dynamics of laser sources have been rigorously studied. The linewidth fundamentally defines the spectral purity of a laser, indicating the range of frequencies over which the laser emits. As a result, significant efforts have been made to systematically understand linewidth behavior, including linewidth broadening factors in semiconductor lasers [19], quantum noise during amplified spontaneous emission [20], and nonlinear conversion processes [21]. Building on the foundational understanding of linewidth and phase noise in conventional lasers, recent research has focused on the unique characteristics of frequency combs. According to the elastic-tape model [22], it has been observed that the frequency noise of comb lines increases quadratically with the mode number from the fixed point [23]. This behavior reflects a systematic broadening of the linewidth across the entire comb spectrum, intrinsically linked to the coherent transduction of the pump laser's noise and the timing jitter fluctuations in the repetition rate [24]. Additionally, further investigations have explored noise behavior and its origins in soliton microcomb dynamics [25], including thermorefractive noise in silicon nitride (Si_3N_4) microresonators [26–28], timing jitter induced by intracavity power fluctuations [29], the linear dependence of comb linewidth on the pump laser [30], and the Quiet Point (QP) analysis based on Raman self-frequency shifts and dispersive-wave soliton recoil [31].

Building on these understandings, recent work has experimentally demonstrated narrow-linewidth lasers on integrated platforms. These lasers maintain a fixed phase relationship over time, ensuring accurate frequency measurements and reducing phase noise. Examples include self-injection-locked coherent optical parametric oscillators [32], hertz-linewidth semiconductor lasers referenced to optical microresonators [33], chip-based optical spiral and ring cavity lasers [34,35], sub-hertz linewidth Brillouin lasers [36], and photonic flywheels [37], with linewidths reaching a few Hz. These linewidth and phase noise improvements enhance the coherence and spectral purity of frequency comb lines, and are crucial for ultra-precision applications like time/frequency transfer [38,39] and high-efficiency coherent communication [40]. To characterize these optical line behaviors, various techniques have been used, including conventional heterodyne detection, short-time delayed linear interferometry [41], self-heterodyne interferometry [42], and self-homodyne interferometry [43], each with different sensitivities and temporal resolutions.

Here, we present a comprehensive study of noise in the microcomb generated from a silicon nitride adiabatic ring microresonator, characterizing linewidth behavior across soliton states of single, double, and soliton crystal configurations. Extending the standard Lugiato-Lefever equation (LLE), we develop a theoretical model to predict dynamics and linewidth broadening, accounting for key noise contributions from thermal noise, shot noise, pump intensity noise, and pump frequency noise. We design and fabricate the adiabatic silicon nitride microresonator, achieving a loaded quality factor of 1.8 million with a width variation from 1 to 4 μm to minimize avoided mode crossings. The path-averaged GVD is near -3 fs^2/mm, with a free spectral range of 88 GHz, as measured using home-built swept-wavelength interferometry. A dual-polarization-driven pump scheme is developed to compensate for thermal effects, ensuring stable soliton formation. We probe the cavity resonance evolution with respect to detuning using the pump phase modulation. Finally, we characterize the linewidths of each soliton state with a short-time delayed linear interferometer (SDLI), revealing kHz-level linewidths in free-running soliton microcombs across the spectrum.

Optics EXPRESS

2. Results

2.1. Soliton microcomb bifurcation diagram and stochastic linewidth calculation

We used the Lugiato-Lefever Equation (LLE) to calculate the bifurcation diagram of our adiabatic ring microcomb. Although the mean-field approximation of the LLE may seem at odds with field fluctuations over the cavity's length scale, our large free spectral range (FSR) relative to the variation in integrated dispersion $D_{int}(\mu, z)$ justifies its use. This ensures that accumulated phase modulation and boundary condition modulation satisfy the mean-field approximation, especially at lower power regimes. The LLE is expressed as:

$$\frac{\partial \tilde{E}(z,\omega)}{\partial z} = -\left[\alpha + \frac{\frac{T_c}{2} + i(\omega_0 - \omega_p)t_R}{L_{cav}} - i\frac{\beta_2(z)}{2}\omega^2\right]\tilde{E}(z,\omega) + i\gamma(z)\mathcal{F}[E(z,t)|E(z,t)|^2] + \frac{\sqrt{T_c}}{L_{cav}}\tilde{E}_{in} \tag{1}$$

where t_R is the round-trip time, z is the propagation distance, $E(z,t)$ is the intracavity electric field, $\tilde{E}_m(z,\omega)$ is its Fourier transform, E_{in} is the external pump field, α is the propagation loss, T_c is the coupling strength, L_{cav} is the cavity length, $\delta = (\omega_0 - \omega_p)t_R$ is the pump-resonance detuning phase, $\beta_2(z)$ is the second-order dispersion coefficient, and γ is the Kerr nonlinear coefficient. The Raman term is omitted due to its negligible effect in our experimental data. The initial condition is seeded by a single soliton state. We conducted simulations of over 5,000 round-trips to ensure convergence. The intra-cavity power from the final round trip was measured and plotted along the z-axis, as shown in Fig. 1(a), revealing the Turing roll, chaotic microcomb, and soliton microcomb regions across the pump power and resonance detuning parameter space. The calculated results align with our experimental observations of single soliton, double soliton, and soliton crystal microcombs.

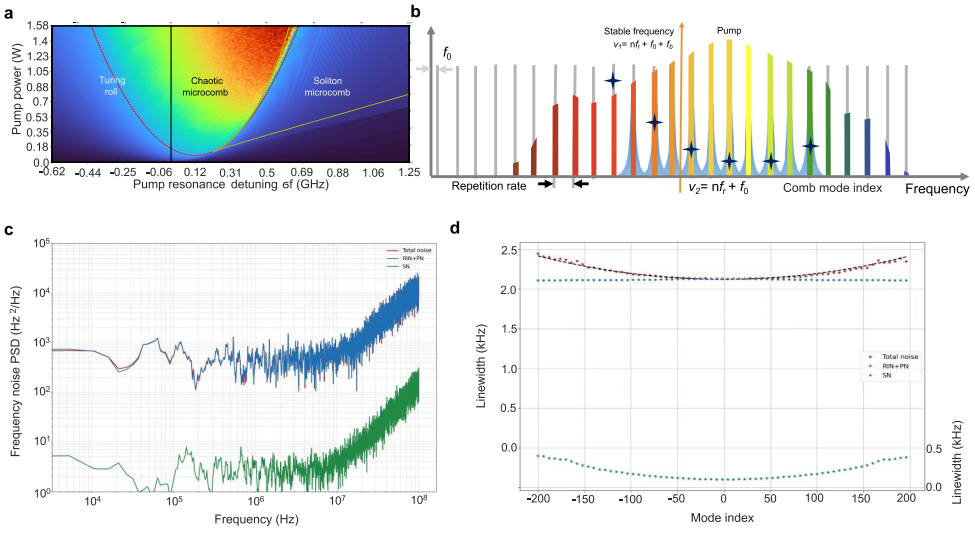

Fig. 1. Soliton microcomb formation in microresonators. (a) Numerically simulated bifurcation diagram of the microcomb. (b) Conceptual illustration showing the overlap of comb lines with the calculated linewidth broadening in the silicon nitride adiabatic ring microresonator. (c) The calculated comb line frequency noise power spectrum density with the different type noise. (d) The calculated linewidth distribution based on the different type noise.

To characterize linewidth performance, we incorporated thermal noise (ϵ_Θ), shot noise (ϵ_s), pump laser intensity noise ($\epsilon_{in,P}$), and phase noise ($\epsilon_{in,\Phi}$) into the Ikeda map model. These noise

Optics EXPRESS

sources are sampled through normal distributions. The standard deviations of $\epsilon_{\mathrm{in,P}}$ and $\epsilon_{\mathrm{in},\Phi}$ are determined by the laser's relative intensity noise (RIN) power spectral density (PSD) and frequency noise PSD, respectively. To extend the simulation's Fourier frequency range to kHz, we performed a total of 2^{24} roundtrips. The resulting linewidth distribution with blue stars for the frequency microcomb is shown in Fig. 1(b). The dynamics are expressed as:

$$\begin{cases} E_{m+1}(0,t) = \sqrt{T_c}(E_{m,in} + \epsilon_{\mathrm{in,P}}) + \sqrt{1-T_c}e^{-i(\omega_0-\omega_p)t_R}E_m(L_{cav},\ t) + \epsilon_{\mathrm{s}} \\ \frac{\partial \tilde{E}_m(z,\omega)}{\partial z} = -\left[\alpha - i\frac{\beta_2(z)}{2}\omega^2 - i\epsilon_\Theta\right]\tilde{E}_m(z,\omega) + i\gamma(z)\tilde{E}_m(z,\omega) \star \{\mathcal{F}[R(t')] \times \mathcal{F}[|E_m(z,t)|^2]\} \end{cases} \tag{2}$$

where the pump intensity noise is modeled by adding a fluctuation term, $\epsilon_{\mathrm{in,P}} = P_{in}\sqrt{S_{RIN} \times FSR/2} \times \eta$, where S_{RIN} is the laser's relative intensity noise and $\eta \sim \mathcal{N}(0,1)$. Phase noise is introduced by the pump $E_{m,\ in} = \sqrt{P_{in}}e^{i\phi_m}$, where $\phi_{m+1} = \phi_m + \epsilon_{\mathrm{in},\Phi}$, $\epsilon_{\mathrm{in},\Phi} = \sqrt{2\pi\Delta\nu_p/FSR} \times \eta$. The shot noise is modeled by $\epsilon_{\mathrm{s}} = P_{in}\sqrt{h\nu_p \times N \times FSR \times T_c} \times (\eta_1 + i\eta_2)$. Temperature variations significantly impact detuning, so thermal noise is included in the detuning term $\epsilon_\Theta = A \times \eta$, where A represents temperature amplitude variations. The calculated stochastic linewidth is shown in Fig. 1(b) with blue stars. The comb line frequency noise power spectrum density is numerically calculated with the pump intensity and phase noise, and the shot noise as shown in Fig. 1(c) for the 44-th comb mode from the pump. We obtained the linewidth distribution with respect to the comb mode number as shown in Fig. 1(d) after integration of the comb line frequency noise PSD.

Microcomb line frequency noise depicts the deviation ($\Delta\nu_{\mathrm{n}}$) of comb lines from the frequency grid, $\nu_{\mathrm{n}} = \mathrm{n}f_{\mathrm{R}} + f_{\mathrm{CEO}}$, where n is the comb mode index across the entire Kerr comb (Fig. 1(b)). The corresponding optical phase deviation is $\Delta\phi_{\mathrm{n}} = 2\pi\Delta\nu_{\mathrm{n}}t$. The optical power spectrum consists of Lorentzian-shaped comb lines [23], expressed as:

$$\tilde{A}(\upsilon) = \frac{|\tilde{a}(\upsilon - \upsilon_p)|^2}{2\pi t_R^2} \sum_n \frac{2\Delta\upsilon_n}{(\upsilon - \upsilon_n)^2 + \Delta\upsilon_n^2} \tag{3}$$

where $\tilde{\mathrm{a}}(\nu)$ is the Fourier transform of the optical pulse envelope, ν_{n} are the comb-line frequencies without frequency fluctuations, and $\Delta\nu_{\mathrm{n}}$ is the linewidth of individual comb lines. Optical phase fluctuations are governed by $\phi(\nu_{\mathrm{n}}+\Delta\nu_{\mathrm{n}}) = \phi(\nu_{\mathrm{n}}) + 2\pi\Delta t_{\mathrm{R}}\Delta\nu_{\mathrm{n}}$. Linewidth and frequency noise are minimized at the central comb lines but increase toward the wings due to repetition rate timing deviations. We apply the well-known elastic tape model to Kerr frequency microcombs and discuss the sources of optical frequency noise. Since all comb lines are mode-locked, their fluctuations occur collectively. Perturbations lead to frequency comb lines "breathing" around a fixed frequency (ν_{fix}), with frequency fluctuations expressed in terms of the offset from this fixed frequency.

2.2. Adiabatic microring implementation and cold cavity dispersion characterization

Figure 2(a) shows the scanning electron microscopy (SEM) of the adiabatic microring cavity. The device fabrication begins with the deposition of a 3 μm thick SiO_2 layer on a p-type 8" silicon wafer via plasma-enhanced chemical vapor deposition (PECVD) to serve as the under-cladding oxide. A subsequent 800 nm silicon nitride layer is deposited via low-pressure chemical vapor deposition (LPCVD), then patterned and etched down to the buried oxide cladding using 248 nm deep-ultraviolet lithography and optimized reactive ion etching. The nitride rings are over-cladded with a 3 μm thick oxide layer, first deposited by LPCVD (0.5 μm) and then by PECVD (2.5 μm). The device studied has a ring radius of 261 μm, with a waveguide width range of 1 to 4 μm. Figures 2(b) and 2(c) show the calculated group velocity dispersion (GVD) and third-order dispersion (TOD) of the microring cavity, obtained using a commercial full-vector finite-element-mode solver (COMSOL Multiphysics), which accounts for both geometric and material dispersion. The calculated GVD and TOD oscillate within the microcavity, ranging

Optics EXPRESS

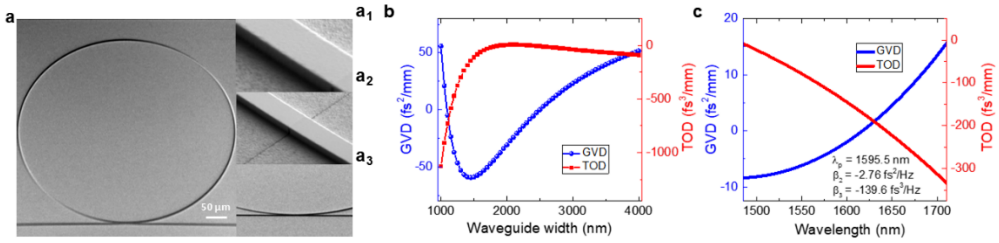

Fig. 2. Adiabatic ring fabrication. (a) Layout of the adiabatic ring cavity with input/output mode converters with less than 3 dB coupling loss on each facet. The zoomed-in views of ring widths ranging from 1 to 4 μm, shown in panels a_1, a_2, and a_3, illustrate the coupling gap between the bus waveguide and the ring cavity. (b) COMSOL modeled GVD and TOD of the Si_3N_4 waveguide with respect to the waveguide width. (c) COMSOL modeled path-averaged GVD and TOD over the entire microcavity which is calculated by $\beta_{i\Sigma} = \int \beta_i dL / L_{cavity}$ based on the data as shown in b.

from 55 to -59 fs^2/mm and -1125 to 6 fs^3/mm, respectively. At the pump wavelength of 1595.5 nm, the fundamental mode (TE_{00}) exhibits a small anomalous path-averaged GVD of -2.76 fs^2/mm and TOD of -139.6 fs^3/mm. Swept-wavelength interferometry was used to characterize the dispersion of the silicon nitride adiabatic ring microresonator, as shown in Fig. 3(a). The free spectral range (FSR) and quality factor (Q-factor) were derived from the microring transmission, measured by sweeping a tunable laser. 1% of the laser output was injected into a fiber-coupled hydrogen cyanide gas cell (Wavelength References Inc.; HCN-13-100) and subsequently into a photodetector for absolute wavelength calibration.

The microcavity and gas cell transmissions are recorded during the laser sweep by a data acquisition system, with the sample clock derived from a photodetector (PD_{MZI}) monitoring the laser transmission through an unbalanced fiber Mach-Zehnder interferometer (MZI). Figure 3(b) shows the microcavity transmission over a wavelength range from 1550 nm to 1610 nm, calibrated by fitting 17 absorption features in the gas cell transmission. The data reveals that the microcavity is single-mode and near critically coupled. The pump resonance at 1595.7 nm is fitted with a Lorentzian lineshape, as shown in Fig. 3(c), yielding a loaded Q-factor of 1.8 million for the cold cavity. An N-Lorentzian fit is then applied to determine the cavity dispersion, where N is the number of resonances fitted. The microring resonator dispersion is calculated by analyzing the wavelength dependence of the FSR, as shown in Fig. 3(d).

2.3. *Dual-polarization-driven thermally stable soliton microcomb generation*

To mitigate thermal effects in the microresonator, we employ a dual-driven, dual-polarization pump technique to stably access different soliton microcomb states. Figure 4(a) illustrates the setup, where the forward-propagating pump laser is amplified and selected into the transverse-electric (TE) polarization at the input polarization beamsplitter, while the backward-propagating transverse-magnetic (TM) polarized auxiliary laser stabilizes the microresonator thermally. The auxiliary laser, set to 1565 nm (blue-detuned region), introduces thermal pre-compensation, decoupling the microresonator's thermal hysteresis from Kerr soliton dynamics. The main pump laser, coupled to a different cavity mode, is initially blue-detuned and gradually tuned to the red-detuned region to generate the soliton microcomb. Figure 4(b) shows the power transmission of both lasers when the microresonator is driven at high power, with the main pump laser frequency scanned over a resonance at a rate of 20 nm/s. The transmission signal, shown by the blue curve, exhibits discrete steps in the effectively red-detuned region, indicating the presence of soliton states. Soliton generation is enhanced by thermal compensation from the auxiliary laser. Figure 4(c) presents optical spectra for different detuning regions, including the

Optics EXPRESS

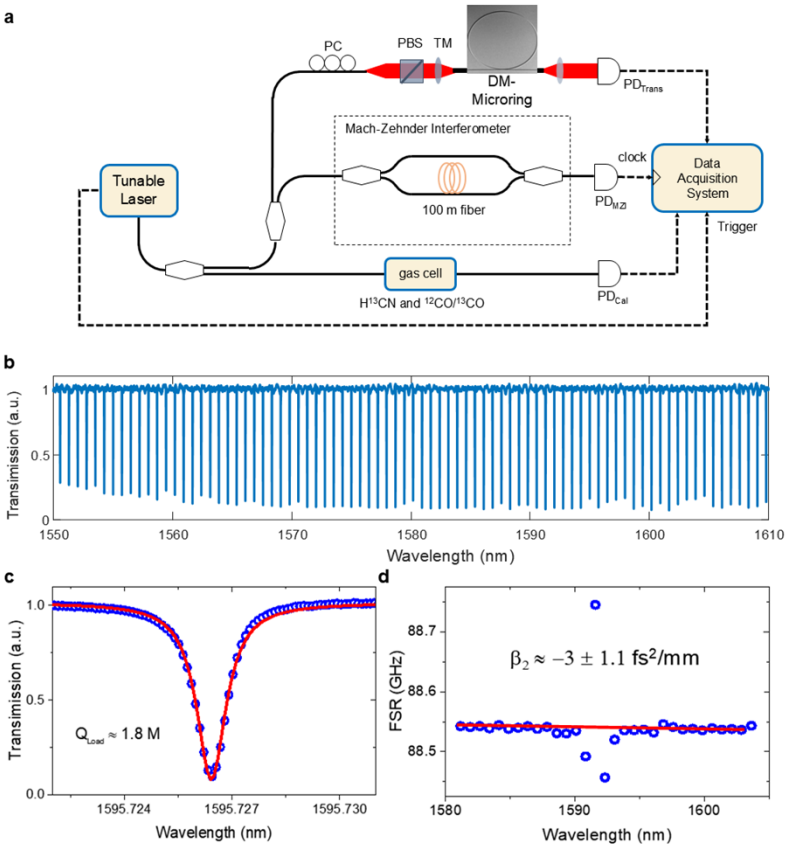

Fig. 3. Dispersion measurement setup based on swept-wavelength interferometry. (a) The laser is swept through its wavelength range from 1510 nm to 1610 nm at 100 nm/s tuning speed and the absolute wavelength is calibrated with a hydrogen cyanide gas cell with 17 absorption features over L-band. A 5 MHz optical frequency sampling resolution is achieved by monitoring the laser transmission through a fiber Mach-Zehnder interferometer with 40 m unbalanced path lengths. (b) The transmission spectrum over 1550 nm to 1610 nm ranges in the microresonator. (c) The enlarged transmission spectrum of 1595.7 nm at the pump, fitted with a Lorentzian lineshape and measured to have Q_{Load} of 1.8 million. (d) The measured anomalous GVD is $\beta_2 = -3 \pm 1.1$ fs^2/mm, and the FSR (D_1) of the device is 88 GHz.

Turing pattern state (c_1), high noise state (c_2), and single-soliton state (c_3). The corresponding RF amplitude noise, measured over a 1 GHz frequency span, is shown in Fig. 4(d), along with the photodetector background. The amplitude noise measurements in Figs. 4(d_2) and 4(d_3) reveal a transition from a high noise state to a low noise soliton state. Once the low noise state is achieved, the RF amplitude noise decreases by over 30 dB, reaching the photodetector noise floor.

2.4. *Dynamics of microcomb soliton generation over pump-resonance detuning with phase-sensitive probing*

Subsequently, we continuously sweep the main pump laser over the resonance while recording the resonance response of the heated cavity using an electrical vector network analyzer (EVNA) to monitor the "*S*-resonance" and "*C*-resonance" originating from the cavity resonance related to the pump CW laser. To thoroughly explore the resonance dynamics, we introduce the effective pump-laser-resonance frequency detuning to identify "*C*-resonance" firstly. The detuing is

Optics EXPRESS

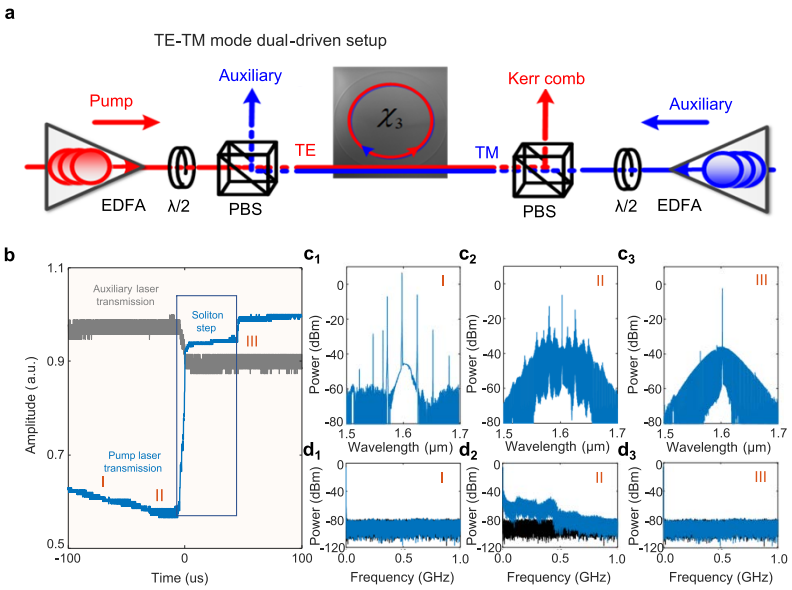

Fig. 4. Dual-polarization-driven thermally stable soliton microcomb generation. (a) TE-TM dual-driven approach. EDFA: erbium-doped fiber amplifier; PBS: polarization beam splitter; TE: transverse-electric; TM: transverse-magnetic; λ/2: half-wave plate. (b) The pump laser transmission follows the expected triangular resonance shape. (c_{1-3}) Frequency microcombs states. (d_{1-3}) Corresponding RF amplitude noise.

defined with the $2\pi\delta_{\text{eff}} = \omega_{\text{T}} - \omega_{\text{p}}$ where ω_{T} is the hot cavity frequency including thermal effect and ω_{p} is the pump frequency. In our experiment, we use absolute wavelength to identify the detuning. Fristly, the pump is in the blue-detuned regime with Lorentzian-like *C*-resonance and evolves to be smaller effective detuning. The entire resonance and optical spectrum evolution for each state are recorded simultaneously under different pump-resonance detuning conditions, as shown in Figs. 5(a) and 5(b). Figures 5(d_{1-2}) illustrate the evolution of the hot resonance as it transitions from blue to red detuning, along with the corresponding cavity and soliton resonance. As shown in Fig. 5(d_1), the *C*-resonance shifts towards the *S*-resonance and leaves away due to the decrease and increase of the pump frequency. The asymmetric resonance resonpose is observed with green curve indicating to access modulational instability regime. Figure 5(d_2) shows the zoomed resonance evolution for the discrete pump frequency. We can observe that the resonance frequency is fixed at 1 pm, 0.5 pm, and 0.25 pm indicating the thermal and Kerr locking of the cavity resonance to the pump frequency. After the laser frequency across the effective zero detuning, double-resonance feature is obsereved with -2 pm in Fig. 5(d_1). The *S*-resonance is recorded due to an additional shift of the cavity resonance resulting from the soliton power-depenedent Kerr phase shift. Figure 5(c) displays the pump power transmission of the heated cavity.

We then turn off the EVNA and record the optical spectral evolution during forward and backward sweeps of the pump-resonance detuning, as shown in Figs. 6(a) and 6(b), demonstrating the effective thermal compensation capability of the TE-TM dual-driven method. The soliton existence range is expanded with the dual-driven method. Different mode-locked states, including single soliton, double soliton, and soliton crystal, are accessed, enabling reliable investigation of linewidth dynamics.

Optics EXPRESS

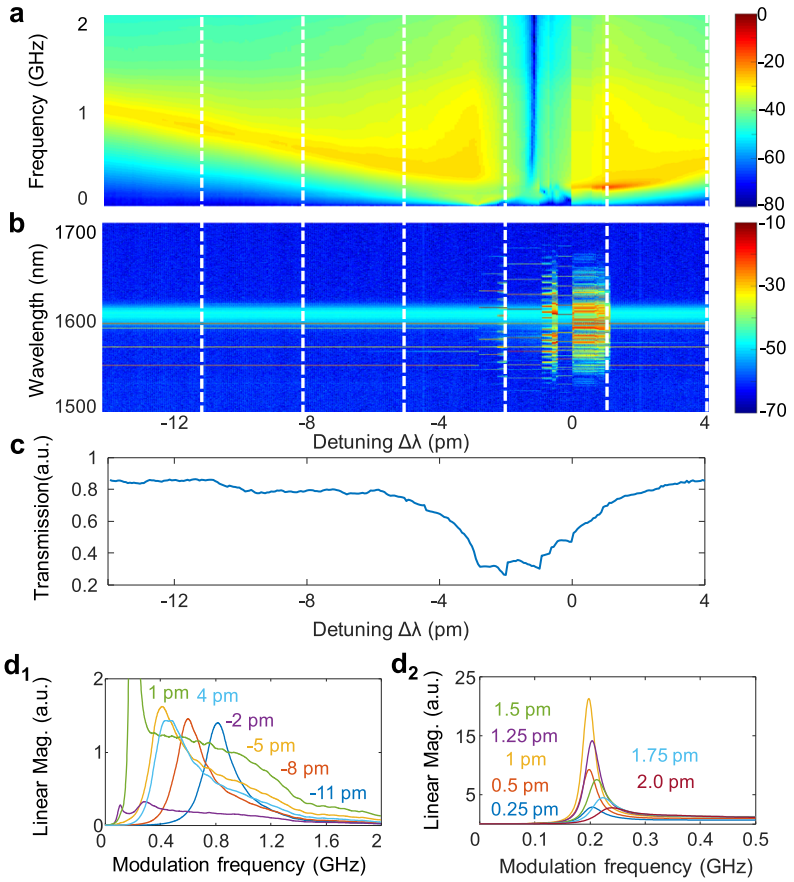

Fig. 5. Hot cavity resonance evolution and pump-resonance detuning measurement. (a) Hot cavity evolution with forward tuning of the pump wavelength. (b) Corresponding optical spectral evolution of the microcomb. (c) Power transmission with respect to absolute pump-resonance detuning. (d_1) Hot resonance evolution from blue to red detuning of the resonance. (d_2) Cavity resonances at different absolute detunings.

2.5. *Interferometric coherence envelope measurements of soliton microcomb instantaneous linewidths*

One of soliton microcomb lines is selected by a 230 pm diffractive grating based tunable optical filter (JDS Uniphase TB9) and then is sent into the short-time delayed linear interferometer (SDLI) to obtain coherent envelopes with different delay times. The coherent envelopes are recorded by an electrical spectrum analyzer (Agilent CXA N9000A) with resolution bandwidth of 10 Hz and a span of 2 MHz, averaged over 50 scans. The input optical power of the SDLI is 500 μW. To further elucidate the noise characteristics of the soliton microcombs, here we investigate instantaneous linewidths of the generated individual comb teeth and soliton microcomb linewidth distributions. We built a SDLI based on Michelson interferometry with heterodyne detection as shown in Fig. 7(a). This approach converts the frequency fluctuation $[\Delta\nu_m=\Delta(f_p+mf_R)=\Delta f_p(1+m\times\Delta f_R/\Delta f_p)]$ of the microcomb lines into the second-peak and second-trough (SPST) power contrast difference (ΔP) of the coherent interference pattern in the SDLI which can be expressed

Optics EXPRESS

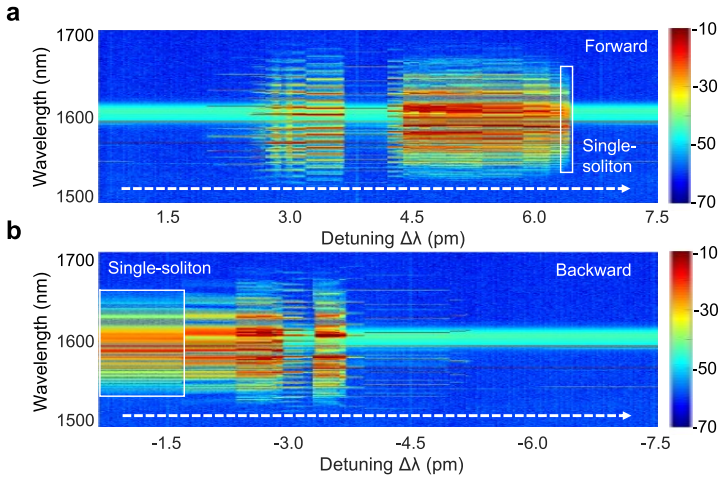

Fig. 6. Optical spectral evolution of the microcomb with forward and backward wavelength tuning for the TE-TM driven soliton generation method. (a) Single-soliton formation with forward wavelength tuning. (b) Transition from single-soliton to multiple soliton states with backward wavelength tuning.

as [41]:

$$\Delta P = 10\log_{10}P_{peak} - 10\log_{10}P_{trough} = 10\log 10\frac{\left[1+\left(\frac{2}{n_0\Delta\nu\tau}\right)^2\right][1+\exp(-2\pi n_0\Delta\nu\tau)]}{\left[1+\left(\frac{3}{2}\frac{1}{n_0\Delta\nu\tau}\right)^2\right][1-\exp(-2\pi n_0\Delta\nu\tau)]} \quad (4)$$

where τ is the delay time, n_0 is the fiber refractive index, and $\Delta\nu$ is the comb mode linewidth. The power spectrum of the SDLI is the product of the Lorentzian spectrum and the periodic modulation power spectrum.

Figure 7(b) shows the measured interferometric coherence envelope power spectrum of the pump laser and one of comb lines with mode number $\mu = 44$ away from the pump. Polynomial curve fitting is used to detect the peaks and troughs of the interference envelope. Figure 7(c) shows the measured and calculated interferometric envelopes at different time delays to evaluate the spectral resolution and power dynamic range. The measured linewidth of the pump laser is 1.5 kHz when the time delay is 3.55 μs, in which the ΔP ranges from 15-20 dB. The measured interferometric envelopes of the single-soliton, double-soliton, and soliton crystal microcombs are presented in Fig. 7(d_1), 7(d_2), and 7(d_3) overlapped with the calculated envelopes at the same time delay showing the microcomb linewidths of 2.3 kHz, 3.0 kHz and 2.4 kHz, respectively. Next, we study the linewidth distribution of microcomb lines over the C-band from 1560 nm to 1570 nm to examine linewidth multiplication away from the pump in soliton frequency microcombs.

Figure 7(e) shows the linewidth distribution for the different microcomb dynamical states with the pump centered at ≈ 1602 nm and in the range of ≈ 10 nm. A slight increase in linewidth further away from the pump towards shorter wavelengths is observed in Fig. 7(e_2) due to the decrease in the comb line optical power from double-pulse spectral interference. In the soliton crystal state, the linewidth distribution has a larger fluctuation which arises from the structured optical spectrum, due to the signal-to-noise ratio dependence of the measurement.

Optics EXPRESS

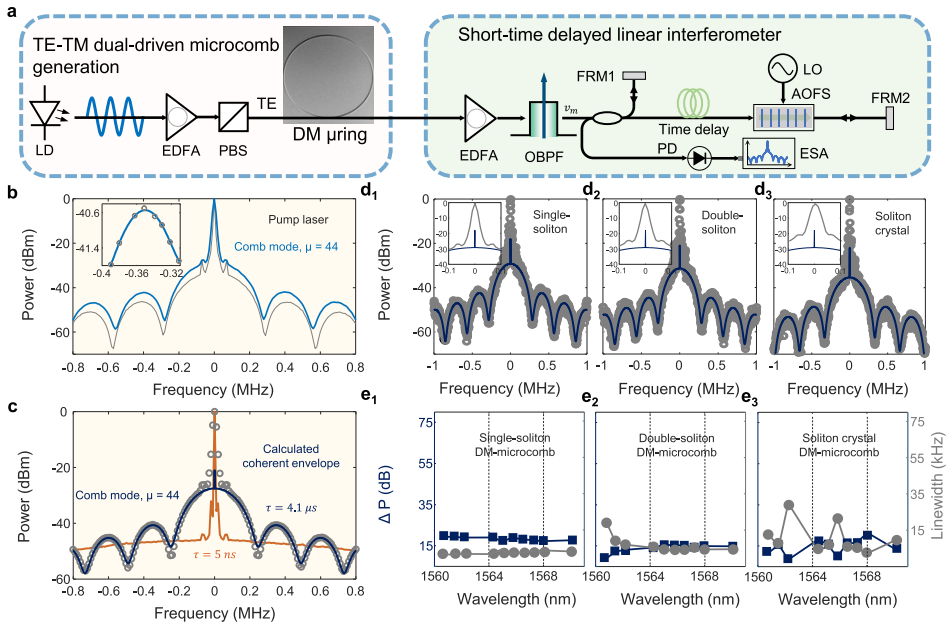

Fig. 7. Near-instantaneous linewidth measurement of the microcomb. (a) Experimental setup of the short-time delayed linear interferometer (SDLI). FRM: Faraday rotator mirror, AOFS: acoustic optical frequency shifter, LO: local oscillator, ESA: electrical spectrum analyzer. (b) Measured interferometric coherence envelope (ICE) of the pump laser and one of microcomb lines ($\mu = 44$). Inset is polynomial curve fitting for peak detection. (c) Measured ICE with different time delays to show spectral resolution and power dynamic range of the SDLI. (d_1), (d_2), and (d_3) Measured ICE of one comb line of the single-soliton, double-soliton and soliton crystal microcombs, respectively. Insets are the zoomed views. (e_1), (e_2), and (e_3) Linewidth distributions of the different comb lines from 1560 nm to 1570 nm for varied soliton comb states. Optical delay length is 50 m.

3. Conclusion

We have successfully designed and fabricated a silicon nitride adiabatic ring microresonator with low average dispersion and negligible avoided mode crossings, making it ideal for microcomb generation. Through detailed numerical simulations and experimental measurements, we explored the soliton microcomb bifurcation diagram and investigated the stochastic linewidth of the generated microcombs. The device demonstrated excellent performance, with a high loaded quality factor and low group velocity dispersion. Using a thermally stabilized dual-polarization-driven method, we demonstrated the formation of single soliton, double soliton, and soliton crystal microcombs, with the ability to tune the pump wavelength in both forward and backward directions. The measured linewidths of individual comb teeth were on the order of 2–3 kHz, with linewidth distributions showing slight increases at shorter wavelengths. This linewidth or optical frequency noise performance is compared with other various frequency comb platforms and listed as Table 1. Note that our narrow linewidth performance is mainly attributed to our pump laser and dual-pump driven soliton scheme, and this can be further improved by locking the pump lasers as demonstrated in [16,33]. These findings highlight the importance of understanding the fundamental linewidths in high-clock-rate microcombs, which is crucial for advancing their use in emerging applications such as precision measurement and optical communication.

Optics EXPRESS

Table 1. | Representative optical frequency noise or linewidth performances of free-running frequency comb.

Laser Solid-state/Fiber/Microcavity	3-dB linewidth	Frequency noise PSD at 10 kHz Fourier frequency (Hz^2/Hz)	Measurement method
100 MHz, Ti:Sapphire laser [44]	–	30	HD
227 MHz, SESAM, Er:Yb-glass laser [45]	several kHz at 10 ms	10^3	FD[a]
250 MHz, NPR, soliton Er-fiber laser [46]	100 kHz	2×10^5	HD
100 MHz, NPR, soliton Yb-fiber laser [47]	65 kHz	1×10^4	HD[a]
227.5 GHz, soliton nitride microcomb [31]	1-6 kHz	$\sim10^5$	HD
97.5 GHz, power-efficient ALGaAsOI Dark-pulse soliton [48]	300 Hz - 40 kHz	$\sim2\times10^4$	HD
88 GHz, dual-driven, soliton nitride microcomb [this work]	2.3 kHz	–	SDLI

[a]HD: Heterodyne detection, FD: Frequency discriminator.

Funding. National Science Foundation (1824568, 1810506, 1741707, 1829071); Office of Naval Research (N00014-16-1-2094).

Disclosures. The authors declare no conflicts of interest.

Data availability. Data used in this study are available from the corresponding author upon reasonable request.

References

1. S. A. Diddams, K. Vahala, and T. Udem, "Optical frequency combs: Coherently uniting the electromagnetic spectrum," Science **369**(6501), 267 (2020).
2. B. C. Yao, W. T. Wang, Z. D. Xie, *et al.*, "Interdisciplinary advances in microcombs: bridging physics and information technology," eLight **4**(1), 19 (2024).
3. T. J. Kippenberg, A. L. Gaeta, M. Lipson, *et al.*, "Dissipative Kerr solitons in optical microresonators," Science **361**(6402), 8083 (2018).
4. Y. Xuan, Y. Liu, L. T. Varghese, *et al.*, "High-Q silicon nitride microresonators exhibiting low-power frequency comb initiation," Optica **3**(11), 1171–1180 (2016).
5. C. Lecaplain, C. Javerzac-Galy, M. L. Gorodetsky, *et al.*, "Mid-infrared ultra-high-Q resonators based on fluoride crystalline materials," Nat. Commun. **7**(1), 13383 (2016).
6. Y. He, Q.-F. Yang, J. Ling, *et al.*, "Self-starting bi-chromatic LiNbO3 soliton microcomb," Optica **6**(9), 1138–1144 (2019).
7. X. Yi, Q.-F. Yang, K. Y. Yang, *et al.*, "Soliton frequency comb at microwave rates in a high-Q silica microresonator," Optica **2**(12), 1078–1085 (2015).
8. M. -G. Suh, Q.-F. Yang, K. Y.L. Yang, *et al.*, "Microresonator soliton dual-comb spectroscopy," Science **354**(6312), 600–603 (2016).
9. L. Lundberg, M. Mazur, A. Mirani, *et al.*, "Phase-coherent lightwave communications with frequency combs," Nat. Commun. **11**(1), 201 (2020).
10. Y. -S. Jang, H. Liu, J. Yang, *et al.*, "Nanometric precision distance metrology via hybrid spectrally resolved and homodyne interferometry in a single soliton frequency microcomb," Phys. Rev. Lett. **126**(2), 023903 (2021).
11. W. Weng, E. Lucas, G. Lihachev, *et al.*, "Spectral Purification of Microwave Signals with Disciplined Dissipative Kerr Solitons," Phys. Rev. Lett. **122**(1), 013902 (2019).
12. E. Lucas, P. Brochard, R. Bouchand, *et al.*, "Ultralow-noise photonic microwave synthesis using a soliton microcomb-based transfer oscillator," Nat. Commun. **11**(1), 374 (2020).
13. A. Aldhafeeri, H.-H. Chin, T. Melton, *et al.*, "Low phase noise K-band signal generation using polarization diverse single-soliton integrated microcombs," Photonics Res. **12**(6), 1175–1185 (2024).
14. S.-W. Huang, J. Yang, S.-H. Yang, *et al.*, "Globally Stable Microresonator Turing Pattern Formation for Coherent High-Power THz Radiation On-Chip," Phys. Rev. X **7**(4), 041002 (2017).

Optics EXPRESS

15. W. Wang, P.-K. Lu, A. K. Vinod, *et al.*, "Coherent terahertz radiation with 2.8-octave tunability through chip-scale photomixed microresonator optical parametric oscillation," Nat. Commun. **13**(1), 5123 (2022).
16. B. Q. Shen, L. Chang, J. Q. Liu, *et al.*, "Integrated turnkey soliton microcombs," Nature **582**(7812), 365–369 (2020).
17. B. Bai, Q. Yang, H. Shu, *et al.*, "Microcomb-based integrated photonic processing unit," Nat. Commun. **14**(1), 66 (2023).
18. H. Shu, L. Chang, Y. Tao, *et al.*, "Microcomb-driven silicon photonic systems," Nature **605**(7910), 457–463 (2022).
19. M. Osinski and J. Buus, "Linewidth broadening factor in semiconductor lasers–An overview," IEEE J. Quantum Electron. **23**(1), 9–29 (1987).
20. J. C. Garrison, H. Nathel, and R. Y. Chiao, "Quantum theory of amplified spontaneous emission: scaling properties," J. Opt. Soc. Am. B **5**(7), 1528–1539 (1988).
21. R. Hui and A. Mecozzi, "Phase noise of four wave mixing in semiconductor lasers," Appl. Phys. Lett. **60**(20), 2454–2456 (1992).
22. H. R. Telle, B. Lipphardt, and J. Stenger, "Kerr-lens, mode-locked lasers as transfer oscillators for optical frequency measurements," Appl. Phys. B **74**(1), 1–6 (2002).
23. J. W. Kim and Y. J. Song, "Ultralow-noise mode-locked fiber lasers and frequency combs: principles, status, and applications," Adv. Opt. Photonics **8**(3), 465–540 (2016).
24. J. J. McFerran, W. C. Swann, B. R. Washburn, *et al.*, "Elimination of pump-induced frequency jitter on fiber-laser frequency combs," Opt. Lett. **31**(13), 1997–1999 (2006).
25. W. T. Wang, A. Aldhafeeri, H. Zhou, *et al.*, "Polarization-diverse soliton transitions and deterministic switching dynamics in strongly-coupled and self-stabilized microresonator frequency combs," Commun. Phys. **7**(1), 279 (2024).
26. G. Huang, E. Lucas, J. Liu, *et al.*, "Thermorefractive noise in silicon-nitride microresonators," Phys. Rev. A **99**(6), 061801 (2019).
27. J. R. Stone and S. B. Papp, "Harnessing dispersion in soliton microcombs to mitigate thermal noise," Phys. Rev. Lett. **125**(15), 153901 (2020).
28. T. E. Drake, J. R. Stone, T. C. Briles, *et al.*, "Thermal decoherence and laser cooling of Kerr microresonator solitons," Nat. Photonics **14**(8), 480–485 (2020).
29. A. B. Matsko and L. Maleki, "On timing jitter of mode locked Kerr frequency combs," Opt. Express **21**(23), 28862–28876 (2013).
30. P. Liao, C. Bao, A. Kordts, *et al.*, "Dependence of a microresonator Kerr frequency comb on the pump linewidth," Opt. Lett. **42**(4), 779–782 (2017).
31. F. Lei, Z. Ye, Ó. B. Helgason, *et al.*, "Optical linewidth of soliton microcombs," Nat. Commun. **13**(1), 3161 (2022).
32. F. Lei, Y. Sun, Ó. B. Helgason, *et al.*, "Self-injection-locked optical parametric oscillator based on microcombs," Optica **11**(3), 420–426 (2024).
33. W. Jin, Q.-F. Yang, L. Chang, *et al.*, "Hertz-linewidth semiconductor lasers using CMOS-ready ultra-high-Q microresonators," Nat. Photonics **15**(5), 346–353 (2021).
34. H. Lee, M.-G. Suh, T. Chen, *et al.*, "Spiral resonators for on-chip laser frequency stabilization," Nat. Commun. **4**(1), 2468 (2013).
35. D. Huang, M. A. Tran, J. Guo, *et al.*, "High-power sub-kHz linewidth lasers fully integrated on silicon," Optica **6**(6), 745–752 (2019).
36. S. Gundavarapu, G. M. Brodnik, M. Puckett, *et al.*, "Sub-hertz fundamental linewidth photonic integrated Brillouin laser," Nat. Photonics **13**(1), 60–67 (2019).
37. K. Jia, X. Wang, D. Kwon, *et al.*, "Photonic Flywheel in a Monolithic Fiber Resonator," Phys. Rev. Lett. **125**(14), 143902 (2020).
38. K. Predehl, G. Grosche, S. M. F. Raupach, *et al.*, "A 920-Kilometer Optical Fiber Link for Frequency Metrology at the 19th Decimal Place," Science **336**(6080), 441–444 (2012).
39. J. Yang, D. Il Lee, D.-C. Shin, *et al.*, "Frequency comb-to-comb stabilization over a 1.3-km free-space atmospheric optical link," Light: Sci. Appl. **11**(1), 253 (2022).
40. S. Beppu, K. Kasai, M. Yoshida, *et al.*, "2048 QAM (66 Gbit/s) single-carrier coherent optical transmission over 150 km with a potential SE of 15.3 bit/s/Hz," Opt. Express **23**(4), 4960–4969 (2015).
41. S. Huang, T. Zhu, M. Liu, *et al.*, "Precise measurement of ultra-narrow laser linewidths using the strong coherent envelope," Sci. Rep. **7**(1), 41988 (2017).
42. Z. Zhao, Z. Bai, D. Jin, *et al.*, "Narrow laser-linewidth measurement using short delay self-heterodyne interferometry," Opt. Express **30**(17), 30600–30610 (2022).
43. H. Ludvigsen, M. Tossavainen, and M. Kaivola, "Laser linewidth measurements using self-homodyne detection with short delay," Opt. Commun. **155**(1-3), 180–186 (1998).
44. F. W. Helbing, G. Steinmeyer, J. Stenger, *et al.*, "Carrier-envelope-offset dynamics and stabilization of femtosecond pulses," Appl. Phys. B **74**(S1), s35–s42 (2002).
45. S. Schilt, N. Bucalovic, L. Tombez, *et al.*, "Frequency discriminators for the characterization of narrow-spectrum heterodyne beat signals: Application to the measurement of a sub-hertz carrier-envelope-offset beat in an optical frequency comb," Rev. Sci. Instrum. **82**(12), 123116 (2011).
46. P. Brochard, S. Schilt, V. J. Wittwer, *et al.*, "Characterizing the carrier-envelope offset in an optical frequency comb without traditional f-to-2f interferometry," Opt. Lett. **40**(23), 5522–5525 (2015).

Optics EXPRESS

47. L. Nugent-Glandorf, T. A. Johnson, Y. Kobayashi, *et al.*, "Impact of dispersion on amplitude and frequency noise in a Yb-fiber laser comb," Opt. Lett. **36**(9), 1578–1580 (2011).
48. H. Shu, L. Chang, C. Lao, *et al.*, "Submilliwatt, widely tunable coherent microcomb generation with feedback-free operation," Adv. Photonics **5**(03), 036007 (2023).